

Neutrino Emission from Supernovae

Hans-Thomas Janka

Abstract Supernovae are the most powerful cosmic sources of MeV neutrinos. These elementary particles play a crucial role when the evolution of a massive star is terminated by the collapse of its core to a neutron star or a black hole and the star explodes as supernova. The release of electron neutrinos, which are abundantly produced by electron captures, accelerates the catastrophic infall and causes a gradual neutronization of the stellar plasma by converting protons to neutrons as dominant constituents of neutron star matter. The emission of neutrinos and antineutrinos of all flavors carries away the gravitational binding energy of the compact remnant and drives its evolution from the hot initial to the cold final state. The absorption of electron neutrinos and antineutrinos in the surroundings of the newly formed neutron star can power the supernova explosion and determines the conditions in the innermost supernova ejecta, making them an interesting site for the nucleosynthesis of iron-group elements and trans-iron nuclei.

In this Chapter the basic neutrino physics in supernova cores and nascent neutron stars will be discussed. This includes the most relevant neutrino production, absorption, and scattering processes, elementary aspects of neutrino transport in dense environments, the characteristic neutrino emission phases with their typical signal features, and the perspectives connected to a measurement of the neutrino signal from a future galactic supernova.

1 Introduction

The paramount importance of neutrinos in the context of stellar core collapse and the question how massive stars achieve to produce supernova (SN) explosions was first pointed out in seminal papers by Colgate and White (1966) and Arnett (1966).

Hans-Thomas Janka
Max Planck Institute for Astrophysics, Karl-Schwarzschild-Str. 1, 85748 Garching, Germany
e-mail: thj@mpa-garching.mpg.de

They recognized that the huge gravitational binding energy of a neutron star is carried away by neutrinos, which are therefore a copious reservoir of energy for the explosion. Approximating the neutron star of mass M_{ns} and radius R_{ns} by a homogeneous sphere with Newtonian gravity, its binding energy, which roughly equals its gravitational energy, can be estimated as

$$E_{\text{b}} \sim E_{\text{g}} \approx \frac{3}{5} \frac{GM_{\text{ns}}^2}{R_{\text{ns}}} \approx 3.6 \times 10^{53} \left(\frac{M_{\text{ns}}}{1.5 M_{\odot}} \right)^2 \left(\frac{R_{\text{ns}}}{10 \text{ km}} \right)^{-1} \text{ erg}. \quad (1)$$

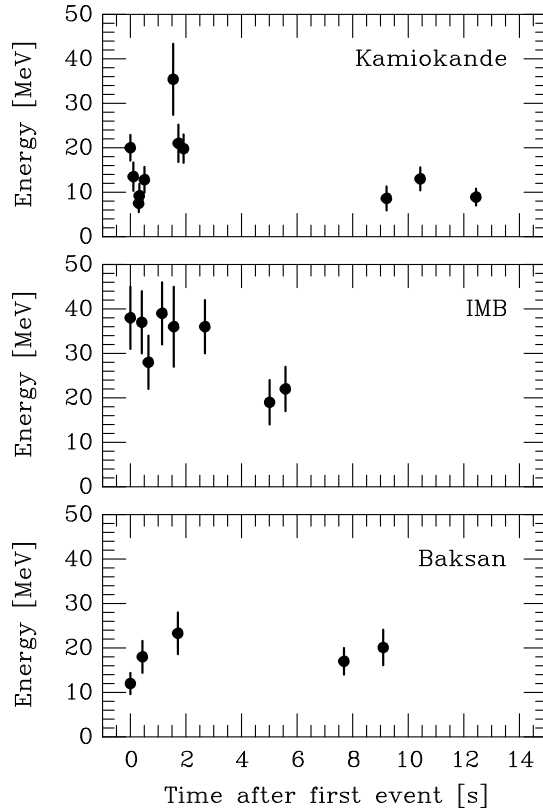
If only a fraction of this energy can be transferred to the gas surrounding the newly formed neutron star, the overlying stellar layers could be accelerated and expelled in a violent blast wave. A major revision of the theoretical picture of neutrino effects in collapsing stars became necessary after weak neutral currents, which had been predicted in theoretical work by Weinberg and Salam, were experimentally confirmed in the early 1970's (Freedman et al, 1977). With neutral-current scatterings of neutrinos off nuclei and free nucleons being possible, it was recognized that the electron neutrinos, ν_e , produced by electron captures can escape freely only at the beginning of stellar core collapse (which starts out at a density around $10^{10} \text{ g cm}^{-3}$), but get trapped to be carried inward with the infalling stellar plasma when the density exceeds a few times $10^{11} \text{ g cm}^{-3}$. At this time the implosion has accelerated so much that the remaining collapse time scale becomes shorter than the outward diffusion time scale of the neutrinos, which increases when scatterings become more and more frequent with growing density. Shortly afterwards, typically around $10^{12} \text{ g cm}^{-3}$, the electron neutrinos equilibrate with the stellar plasma and fill up their phase space to form a degenerate Fermi gas. During the remaining collapse until nuclear saturation density (about $2.7 \times 10^{14} \text{ g cm}^{-3}$) is reached, and the incompressibility of the nucleonic matter due to the repulsive part of the nuclear force enables the formation of a neutron star, the entropy and the lepton number (electrons plus electron neutrinos) of the infalling gas (stellar plasma plus trapped neutrinos) remain essentially constant. Since the change of the entropy by electron captures and ν_e escape until trapping is modest, it became clear that the collapse of a stellar core proceeds nearly adiabatically (for a review, see Bethe, 1990).

The proto-neutron star, i.e., the hot, mass-accreting, still proton- and lepton-rich predecessor object of the final neutron star, with its super-nuclear densities and extreme temperatures of up to several 10^{11} K (corresponding to several 10 MeV) is highly opaque to all kinds of (active) neutrinos and antineutrinos. Neutrinos, once generated in this extreme environment, are frequently re-absorbed, re-emitted, and scattered before they can reach semi-transparent layers near the “surface” of the proto-neutron star, which is marked by an essentially exponential decline of the density over several orders of magnitude. Before they finally decouple from the stellar medium closely above this region and escape, neutrinos have experienced billions of interactions on average. The period of time over which the nascent neutron star is able to release neutrinos with high luminosities until its gravitational binding energy (Eq. 1) is radiated away therefore lasts many seconds (Burrows and Lattimer, 1986; Burrows, 1990a).

This expectation was splendidly confirmed by the first and so far only detection of neutrinos from a stellar collapse on February 23, 1987, in the case of SN 1987A in the Large Magellanic Cloud at a distance of roughly 50 kpc (Raffelt, 1996). The two dozen neutrino events in the three underground experiments of Kamiokande II (Hirata et al, 1987), Irvine-Michigan-Brookhaven (IMB; Bionta et al, 1987), and Baksan (Alexeyev et al, 1988) were recorded over a time interval of about 12 seconds (Fig. 1). Also their individual energies (up to 40 MeV) and the associated integrated energy of the neutrino signal (some 10^{53} erg) were in the ballpark of model predictions and evidenced the birth of a neutron star in this supernova. Figure 2 displays a schematic representation of the neutrino emission that drives the evolution from the onset of stellar core collapse to the cooling of the nascent neutron star, finally leading to a neutrino-transparent neutron star with central temperature below about 1 MeV (roughly 10^{10} K) within some tens of seconds.

The neutrino-interaction processes and basic physics of neutrino transport in supernova matter will be described in Sect. 2, the neutrino-emission phases and corresponding neutrino effects in Sect. 3, and the neutrino-emission properties during the different phases in Sect. 4. Conclusions and an outlook will follow in Sect. 5.

Fig. 1 Neutrino events recorded by the Kamiokande, IMB and Baksan underground experiments. The energies do not refer to the primary electron antineutrinos but to the secondary positrons produced by the captures of such neutrinos on protons, $\bar{\nu}_e + p \rightarrow n + e^+$. The detector clocks had unknown relative offsets; while the absolute timing at IMB had an accuracy of ± 50 ms, the clock at Kamiokande was accurate only to within ± 1 min, and the time measurement at Baksan had an uncertainty of $+2/-54$ s. In the plots the first measured events are synchronized to $t = 0$. (Figure courtesy of Georg Raffelt)



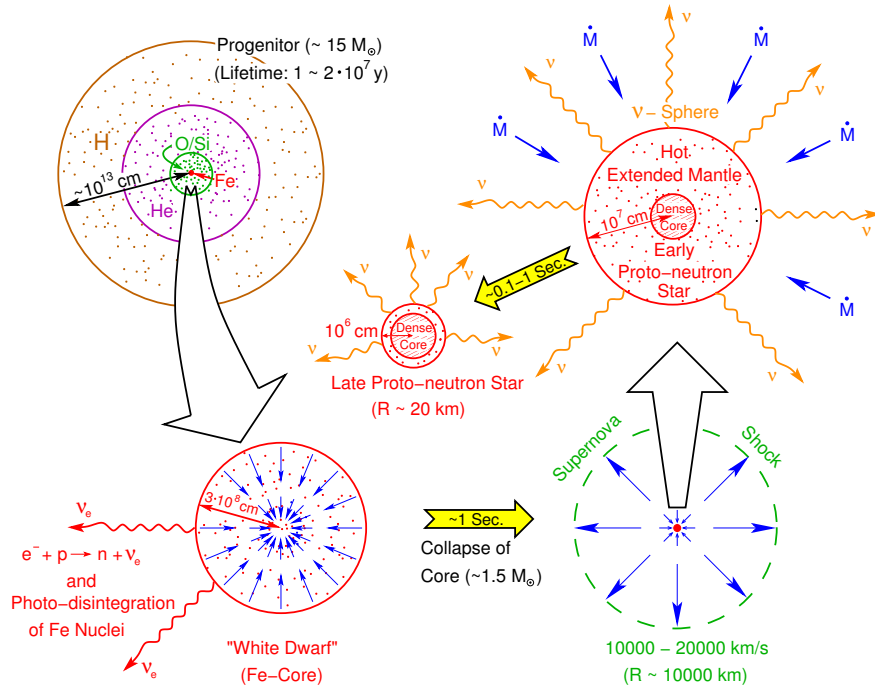


Fig. 2 Evolution of a massive star from the onset of iron-core collapse to a neutron star. The progenitor has developed a typical onion-shell structure with layers of increasingly heavier elements surrounding the iron core at the center (upper left corner). Like a white dwarf star, this iron core (enlarged on the lower left side) is stabilized mostly by the fermion pressure of nearly degenerate electrons. It becomes gravitationally unstable when the rising temperatures begin to allow for partial photo-disintegration of iron-group nuclei to α -particles and nucleons. The contraction accelerates to a dynamical collapse by electron captures on bound and free protons, releasing electron neutrinos (ν_e), which initially escape freely. Only fractions of a second later, the catastrophic infall is stopped because nuclear-matter density is reached and a proto-neutron star begins to form. This gives rise to a strong shock wave which travels outward and disrupts the star in a supernova explosion (lower right). The nascent neutron star is initially very extended (enlarged in the upper right corner), and contracts to a more compact object while accreting more matter (visualized by the mass-accretion rate \dot{M}) within the first second of its evolution. This phase as well as the subsequent cooling and neutronization of the compact remnant are driven by the emission of neutrinos and antineutrinos of all flavors (indicated by the symbol ν), which diffuse out from the dense and hot super-nuclear core over tens of seconds. (Figure adapted from Burrows, 1990b)

2 Neutrino Production and Propagation in Supernova Cores

In collapsing stars neutrinos and antineutrinos of all flavors are produced and absorbed by a variety of processes, and, once created, they scatter off the target particles contained by the stellar medium as well as off neutrinos, whose number densities can exceed those of nucleons and charged leptons in some regions of the su-

Table 1 Most important neutrino processes in supernova and proto-neutron star matter.

Process	Reaction ^a
Beta-processes (direct URCA processes)	
electron and ν_e absorption by nuclei	$e^- + (A, Z) \longleftrightarrow (A, Z-1) + \nu_e$
electron and ν_e captures by nucleons	$e^- + p \longleftrightarrow n + \nu_e$
positron and $\bar{\nu}_e$ captures by nucleons	$e^+ + n \longleftrightarrow p + \bar{\nu}_e$
“Thermal” pair production and annihilation processes	
Nucleon-nucleon bremsstrahlung	$N + N \longleftrightarrow N + N + \nu + \bar{\nu}$
Electron-positron pair process	$e^- + e^+ \longleftrightarrow \nu + \bar{\nu}$
Plasmon pair-neutrino process	$\tilde{\gamma} \longleftrightarrow \nu + \bar{\nu}$
Reactions between neutrinos	
Neutrino-pair annihilation	$\nu_e + \bar{\nu}_e \longleftrightarrow \nu_x + \bar{\nu}_x$
Neutrino scattering	$\nu_x + \{\nu_e, \bar{\nu}_e\} \longleftrightarrow \nu_x + \{\nu_e, \bar{\nu}_e\}$
Scattering processes with medium particles	
Neutrino scattering with nuclei	$\nu + (A, Z) \longleftrightarrow \nu + (A, Z)$
Neutrino scattering with nucleons	$\nu + N \longleftrightarrow \nu + N$
Neutrino scattering with electrons and positrons	$\nu + e^\pm \longleftrightarrow \nu + e^\pm$

^a N means nucleons, i.e., either n or p , $\nu \in \{\nu_e, \bar{\nu}_e, \nu_\mu, \bar{\nu}_\mu, \nu_\tau, \bar{\nu}_\tau\}$, $\nu_x \in \{\nu_\mu, \bar{\nu}_\mu, \nu_\tau, \bar{\nu}_\tau\}$

pernova core. The most important interactions at supernova and proto-neutron star conditions are summarized in Table 1 and Fig. 3.

2.1 Basic Weak Interaction Theory

According to the Weinberg-Salam-Glashow theory (WSG), the weak force between fermions is mediated by the exchange of massive vector bosons, namely two charged intermediate bosons, W^+ and W^- , and one neutral intermediate boson, the Z^0 . Since the interaction energies at typical supernova and proto-neutron star conditions are much smaller than the rest-mass energies of the W and Z bosons, the WSG Hamiltonian density can be rewritten to an effective four-fermion point-interaction V–A Hamiltonian (V stands for the vector part of the interaction, A for the axial-vector part) of the form

$$\mathcal{H}_{\text{weak}} = \frac{G_F}{\sqrt{2}} J_\mu^\dagger J^\mu, \quad (2)$$

where J_μ is the 4-current density of the interacting fermions and G_F is the universal Fermi coupling constant, $G_F = 1.16637 \times 10^{-5} \text{ GeV}^{-2} = 1.43588 \times 10^{-49} \text{ erg cm}^3$ (for unit convention of Planck’s constant $\hbar = h/(2\pi) = 1$ and speed of light $c = 1$). To lowest non-vanishing order the matrix element of the interaction, \mathcal{M} , becomes (e.g. Tubbs and Schramm, 1975; Bruenn, 1985):

$$\mathcal{M}(f + \nu \rightarrow f' + \nu') = \frac{G_F}{\sqrt{2}} \bar{\Psi}_{f'} \gamma_\mu (C_V - C_A \gamma_5) \Psi_f \bar{\Psi}_{\nu'} \gamma^\mu (1 - \gamma_5) \Psi_\nu. \quad (3)$$

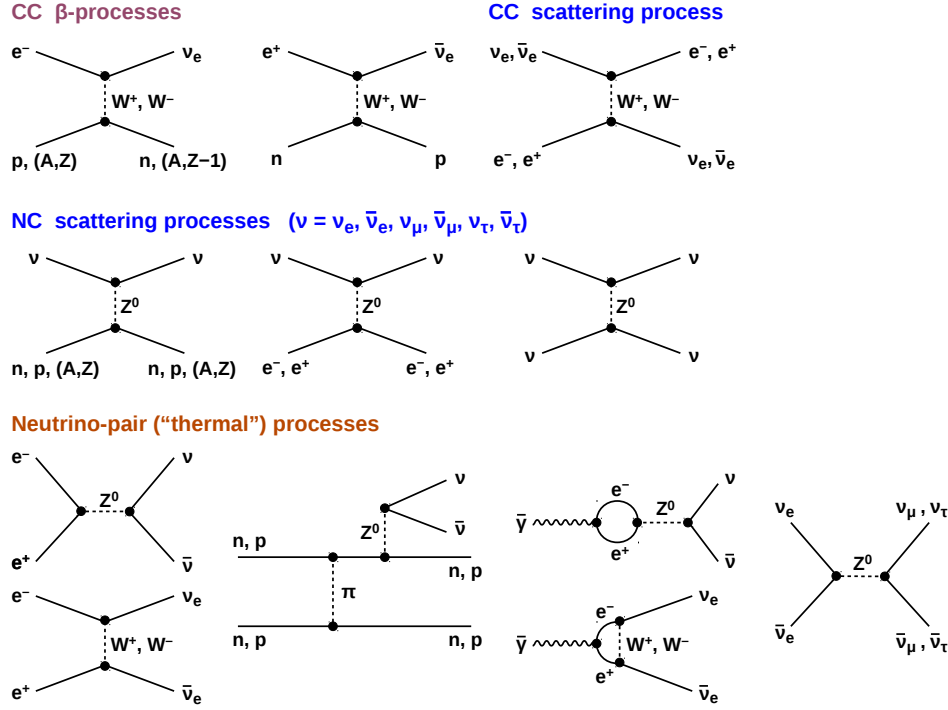


Fig. 3 Feynman diagrams for the lowest-order contributions to the most relevant neutrino interactions in supernova cores. Charged-current (CC) reactions are mediated by W^\pm bosons, neutral-current (NC) reactions by electrically neutral Z^0 bosons. The charged-current β -processes are responsible for the production and absorption of ν_e and $\bar{\nu}_e$ by lepton-capture reactions on nucleons (*top row, left*). Scattering processes include the charged-current interactions of ν_e and $\bar{\nu}_e$ with electrons and positrons (*top row, right*) and neutral-current scatterings of neutrinos and antineutrinos of all flavors with nuclei, neutrons, protons, electrons, positrons, and neutrinos (*middle row*). Neutrino-pair processes are responsible for the creation and annihilation of neutrino-antineutrino pairs of all flavors. They include electron-positron pair annihilation through neutral and charged currents, nucleon bremsstrahlung, the charged- and neutral-current plasmon-neutrino processes, and neutrino-pair conversion between different flavors (*bottom row, from left to right*).

Thus expressing low-energy scattering reactions by an effective neutral-current interaction includes a Fierz-transformed contribution from W exchange when f is a charged lepton and ν the corresponding neutrino. In the case of charged-current electron and positron captures and the inverse ν_e and $\bar{\nu}_e$ absorptions, f and f' denote the incoming and outgoing nucleons and ν and ν' the neutrino and charged lepton in the initial and final states. The compound effective coupling coefficients for the interaction matrix element of Eq. (3) are listed in Table 2 (see also Raffelt, 2012).

With the matrix element being provided by Eq. (3), the reaction rate, \mathcal{R} , of a neutrino of energy q_0 results from integrating the quantity (σu) (having dimensions of $\text{cm}^3 \text{s}^{-1}$) over the initial states of the target particle ($\hbar = c = 1$):

Table 2 Effective coupling coefficients in the weak interaction matrix element of Eq. (3). For the effective weak mixing angle a value of $\sin^2 \theta_W = 0.23146$ was used^a.

Fermion $f (f')$	Neutrino (Lepton)	C_V	C_A	C_V^2	C_A^2
electron	ν_e	$+1/2 + 2 \sin^2 \theta_W$	$+1/2$	0.9272	0.25
	$\nu_{\mu, \tau}$	$-1/2 + 2 \sin^2 \theta_W$	$-1/2$	0.0014	0.25
proton	$\nu_{e, \mu, \tau}$	$+1/2 - 2 \sin^2 \theta_W$	$+1.26/2$	0.0014	0.40
neutron	$\nu_{e, \mu, \tau}$	$-1/2$	$-1.26/2$	0.25	0.40
neutrino (ν_a)	ν_a	$+1$	$+1$	1.00	1.00
	$\nu_{b \neq a}$	$+1/2$	$+1/2$	0.25	0.25
neutron (proton)	ν_e (electron)	$+1.00$	$+1.26$	1.00	1.59
proton (neutron)	$\bar{\nu}_e$ (positron)	$+1.00$	$+1.26$	1.00	1.59

^a For neutrinos interacting with the same flavor, a factor 2 for an exchange amplitude for identical fermions was applied. Possible strange-quark contributions to the nucleon spin were not taken into account for neutral-current neutrino-nucleon scattering. (Table adapted from Raffelt, 2012)

$$\mathcal{R} = \int \frac{d^3 p}{(2\pi)^3} \mathcal{F}(p_0)(\sigma u), \quad (4)$$

where (σu) is the integral over final momentum states of the squared matrix element, summed over final spins and averaged over initial spins:

$$\sigma u \equiv \frac{(2\pi)^{-2}}{2p_0 2q_0} \int \frac{d^3 p'}{2p'_0} [1 - \mathcal{F}(p'_0)] \int \frac{d^3 q'}{2q'_0} [1 - \mathcal{F}(q'_0)] \left(\frac{1}{2} \sum_{\text{spins}} |\mathcal{M}|^2 \right) \delta^4(p + q - p' - q') \quad (5)$$

(Tubbs and Schramm, 1975; Burrows et al, 2006). Here, q and q' are the four-momenta of the incoming and outgoing lepton, respectively, p and p' the four-momenta of the interacting fermions in the initial and final states, q_0 , q'_0 , p_0 , and p'_0 the positive time components (energies) of the four-momenta, and $\mathcal{F}(E)$ the phase-space occupation functions of fermions of energy E . While the medium particles are in equilibrium and their phase-space occupation is described by Fermi-Dirac distributions, the neutrino distribution can be arbitrary. The magnitude of weak interactions is determined by the reference values for the reaction rate and cross section given by

$$\mathcal{R}_0 \equiv \frac{\pi}{2} c \left(\frac{m_e c^2}{2\pi \hbar c} \right)^3 \sigma_0 = 3.297 \times 10^{39} \sigma_0 \text{ cm}^{-2} \text{ s}^{-1}, \quad (6)$$

$$\sigma_0 \equiv \frac{4}{\pi} G_F^2 \frac{(m_e c^2)^2}{(\hbar c)^4} = 1.761 \times 10^{-44} \text{ cm}^2, \quad (7)$$

respectively. Since the squared matrix element is independent of energy, the phase space integration yields a quadratic dependence of the weak interaction cross sections on the particle energy to leading order,

$$\sigma(E) \propto \sigma_0 \left(\frac{E}{m_e c^2} \right)^2. \quad (8)$$

Because of this strong energy dependence of weak interactions, high-energy neutrinos react much more frequently with medium particles by scattering and absorption processes and therefore decouple from the stellar background at a lower density than neutrinos with lower energies. The mean free path between two interactions, is given by $\lambda(E) = (\sum_i n_{t,i} \sigma_i(E))^{-1} \equiv (\rho \kappa_{\text{tot}}(E))^{-1}$, where $n_{t,i}$ is the number density of target particles of species i , $\sigma_i(E)$ the corresponding interaction cross section with neutrinos, ρ the matter density, and $\kappa_{\text{tot}}(E)$ the total opacity in units of $\text{cm}^2 \text{g}^{-1}$. When $\lambda(E)$ includes contributions from all neutrino interactions, neutrino decoupling takes place at the neutrinospheric radius $R_v(E)$ defined as the radial position where the optical depth is unity:

$$\tau_v(E) = \int_{R_v(E)}^{\infty} \frac{dr}{\lambda(r, E)} = \int_{R_v(E)}^{\infty} dr \rho(r) \kappa_{\text{tot}}(r, E) = 1. \quad (9)$$

Frequent scatterings as well as absorption and re-emission induce a random-walk motion of the neutrinos on their way out of the deep interior to the neutrino transparent regime at low densities. Over a (small) vertical distance Δz to the surface, neutrinos of energy E experience an average number of N_{ia} collisions with target particles, which is given by the relation:

$$N_{\text{ia}}^{1/2} \lambda(E) = \Delta z \sim \tau_v(E) \lambda(E). \quad (10)$$

The neutrinosphere at $\tau_v(E) = 1$ is therefore defined as the location where neutrinos of energy E undergo on average one final interaction, $N_{\text{ia}} = 1$, prior to escape.

2.2 Neutrino Transport

Neutrino transport in supernova cores involves a diffusive mode of propagation at the high densities of the newly formed neutron star, a gradual and energy-dependent decoupling of the neutrinos in the neutrinospheric region, and the transition to free streaming when the neutrinos escape from the neutron star. The evolution of the neutrino phase-space distribution function $\mathcal{F}(\mathbf{r}, \mathbf{q}, t)$ in these different regimes is described by the Boltzmann transport equation (e.g. Burrows et al, 2000; Liebendörfer et al, 2001, 2004; Rampp and Janka, 2002; Mezzacappa et al, 2004),

$$\frac{D\mathcal{F}(\mathbf{r}, \mathbf{q}, t)}{Dt} = \frac{\partial \mathcal{F}}{\partial t} + \frac{\partial \mathbf{r}}{\partial t} \nabla_{\mathbf{r}} \mathcal{F} + \frac{\partial \mathbf{q}}{\partial t} \nabla_{\mathbf{q}} \mathcal{F} = \mathcal{C}(\mathcal{F}), \quad (11)$$

where D/Dt denotes the total derivative of $\mathcal{F}(\mathbf{r}, \mathbf{q}, t)$ with respect to time t . $\nabla_{\mathbf{r}}$ and $\nabla_{\mathbf{q}}$ are the partial derivatives with respect to the space coordinates, \mathbf{r} , and momentum coordinates, $\mathbf{q} = q\mathbf{n}$, when \mathbf{n} defines the unit vector in the direction of neutrino

propagation. On the r.h.s. of Eq. (11), $\mathcal{C}(\mathcal{F})$ stands for the collision integral that contains all rates of neutrino production, absorption, annihilation, and scattering processes. Moreover, since supernova neutrinos possess typical energies in the MeV range, which is much larger than the experimental rest-mass limit for active flavors, $m_\nu c^2 < 1$ eV, they propagate essentially with the speed of light c . Therefore one can use $|\mathbf{q}| = q = E/c$ and $\partial \mathbf{r} / \partial t = c \mathbf{n}$. The momentum derivative in Eq. (11), $\partial \mathbf{q} / \partial t$, accounts for the effects of forces on the neutrino, e.g. in the form of gravitational redshifting.

Note that for reasons of simplicity, Eq. (11) was written in a flat spacetime. In practice, the solution of this equation faces a lot of complications not only due to spacetime curvature in general relativity. For the most general case, where non-isoeenergetic scattering redistributes neutrinos in energy-momentum space, Eq. (11) is an integro-differential equation. Final-state fermion blocking and neutrino-antineutrino coupling in pair processes and neutrino-neutrino scattering (Table 1 and Fig. 3) make the problem non-linear in \mathcal{F} . Moreover, the motion of the stellar fluid has to be accounted for by Lorentz transformations and requires the choice of solving for \mathcal{F} in the comoving frame of the fluid, where the collision integral is most easily treated, or in the laboratory frame, where the left-hand side of Eq. (11) retains its simple form.

With the neutrino phase-space distribution function \mathcal{F} being determined as solution of Eq. (11), the quantities characterizing the neutrino emission can be computed as integrals over the coordinates of the momentum vector $\mathbf{q} = (E/c)\mathbf{n}$. This yields for the specific neutrino number density, dn_ν/dE , specific energy density, $d\varepsilon_\nu/dE$, specific number flux, dF_n/dE , specific energy flux, dF_e/dE , and for the corresponding total number and energy densities and fluxes (taking into account that there is one spin state of either left-handed neutrinos or right-handed antineutrinos):

$$\frac{dn_\nu(\mathbf{r}, E, t)}{dE} = \frac{1}{(hc)^3} E^2 \int_{4\pi} d\Omega \mathcal{F}(\mathbf{r}, \mathbf{q}, t), \quad (12)$$

$$\frac{d\varepsilon_\nu(\mathbf{r}, E, t)}{dE} = \frac{1}{(hc)^3} E^3 \int_{4\pi} d\Omega \mathcal{F}(\mathbf{r}, \mathbf{q}, t), \quad (13)$$

$$\frac{dF_n(\mathbf{r}, E, t)}{dE} = \frac{c}{(hc)^3} E^2 \int_{4\pi} d\Omega \mathbf{n} \mathcal{F}(\mathbf{r}, \mathbf{q}, t), \quad (14)$$

$$\frac{dF_e(\mathbf{r}, E, t)}{dE} = \frac{c}{(hc)^3} E^3 \int_{4\pi} d\Omega \mathbf{n} \mathcal{F}(\mathbf{r}, \mathbf{q}, t), \quad (15)$$

$$n_\nu(\mathbf{r}, t) = \int_0^\infty dE \frac{dn_\nu}{dE}, \quad \varepsilon_\nu(\mathbf{r}, t) = \int_0^\infty dE \frac{d\varepsilon_\nu}{dE}, \quad (16)$$

$$\mathbf{F}_n(\mathbf{r}, t) = \int_0^\infty dE \frac{dF_n}{dE}, \quad \mathbf{F}_e(\mathbf{r}, t) = \int_0^\infty dE \frac{dF_e}{dE}, \quad (17)$$

where $d\Omega$ is the solid angle element around unit vector \mathbf{n} . The flux through an area with normal unit vector \mathbf{m} is given by $\mathbf{F}\mathbf{m}$, and the ratio of neutrino flux and neutrino density yields the so-called flux or streaming factor, $s_n = \mathbf{F}_n/(n_\nu c)$ and $s_e = \mathbf{F}_e/(\varepsilon_\nu c)$. The energy moments of order k (i.e., the average values of E^k) for

the local neutrino number density, $\langle E^k \rangle$, and for the neutrino number flux, $\langle E^k \rangle_{\text{flux}}$, are given by:

$$\langle E^k \rangle = \int_0^\infty dE E^{2+k} \int_{4\pi} d\Omega \mathcal{F}(\mathbf{r}, \mathbf{q}, t) \cdot \left\{ \int_0^\infty dE E^2 \int_{4\pi} d\Omega \mathcal{F}(\mathbf{r}, \mathbf{q}, t) \right\}^{-1}, \quad (18)$$

$$\langle E^k \rangle_{\text{flux}} = \left| \int_0^\infty dE E^{2+k} \int_{4\pi} d\Omega \mathbf{n} \mathcal{F}(\mathbf{r}, \mathbf{q}, t) \right| \cdot \left| \int_0^\infty dE E^2 \int_{4\pi} d\Omega \mathbf{n} \mathcal{F}(\mathbf{r}, \mathbf{q}, t) \right|^{-1}. \quad (19)$$

The rms energies of neutrino energy density and neutrino energy flux are defined as $\langle E \rangle_{\text{rms}} = \sqrt{\langle E^3 \rangle / \langle E \rangle}$ and $\langle E \rangle_{\text{rms,flux}} = \sqrt{\langle E^3 \rangle_{\text{flux}} / \langle E \rangle_{\text{flux}}}$.

Since the solution of the time-dependent Boltzmann equation in three spatial dimensions with its full energy-momentum dependence is not feasible on current supercomputers, a variety of different approximations are applied, for example by reducing the number of momentum-space variables by one in the so-called “ray-by-ray” approach (Buras et al, 2006), which assumes the neutrino phase-space distribution \mathcal{F} to be axi-symmetric around one, typically the radial, direction and thus ignores non-radial flux components. Alternatively, the dependence of the Boltzmann equation on the momentum directions can be removed by integration over all directions after multiplication with different powers of \mathbf{n} , by which means an infinite set of so-called moment equations is derived, in which angular moments (integrals) of \mathcal{F} (like those of Eqs. 12–15) appear as dependent variables. Because on each level more moments than equations occur, a termination of the set on any level requires to involve a closure relation, which in most cases is a chosen function between the available moments. A termination on the level of the first moment equation, which is the neutrino energy equation, leads to the diffusion treatment. The compatibility of the diffusion flux (which diverges in the transparent regime) with the causality limit is usually ensured by the use of a flux limiter (e.g. Bruenn, 1985). A termination on the level of the second moment equation, which is the neutrino momentum equation, yields the so-called two-moment transport approximation.

2.3 Flavor-dependent Neutrino Decoupling

Since electrons and positrons are very abundant at the temperatures in supernova cores, whereas muons and taus with their high rest masses are not, ν_e and $\bar{\nu}_e$ interact not only by neutral-current processes but also via charged-current reactions (Tables 1 and 2; Fig. 3). This causes distinct differences of their transport behavior compared to heavy-lepton neutrinos ($\nu_x = \nu_\mu, \bar{\nu}_\mu, \nu_\tau, \bar{\nu}_\tau$), in particular concerning their decoupling near the neutrinosphere.

Charged-current β -processes provide a major contribution to the total opacity of ν_e and $\bar{\nu}_e$, because the interaction cross sections of these reactions are big. Frequent captures and re-emission of these neutrinos at the local conditions of temperature and density are efficient in keeping them fairly close to local thermodynamic equilibrium (i.e., near thermal and chemical equilibrium) until they begin their transi-

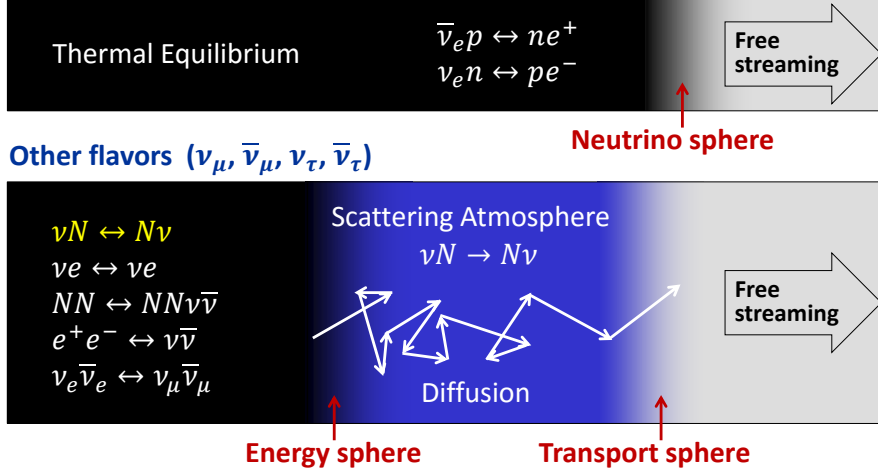
Electron flavor (ν_e and $\bar{\nu}_e$)

Fig. 4 Sketch of the transport properties of electron-flavor neutrinos and antineutrinos (*upper part*) compared to heavy-lepton neutrinos (*lower part*). In the supernova core ν_e and $\bar{\nu}_e$ interact with the stellar medium by charged-current absorption and emission reactions, which provide a major contribution to their opacities and lead to a strong energetic coupling up to the location of their neutrinospheres, outside of which both chemical equilibrium between neutrinos and stellar matter (indicated by the black region) and diffusion cannot be maintained. In contrast, heavy-lepton neutrinos are energetically less tightly coupled to the stellar plasma, mainly by pair creation reactions like nucleon bremsstrahlung, electron-positron annihilation and $\nu_e \bar{\nu}_e$ annihilation. The total opacity, however, is determined mostly by neutrino-nucleon scatterings, whose small energy exchange per scattering does not allow for an efficient energetic coupling. Therefore heavy-lepton neutrinos fall out of thermal equilibrium at an energy sphere that is considerably deeper inside the nascent neutron star than the transport sphere, where the transition from diffusion to free streaming sets in. The blue band indicates the scattering atmosphere where the heavy-lepton neutrinos still collide frequently with neutron and protons and lose some of their energy, but cannot reach equilibrium with the background medium any longer. (Figure adapted from Raffelt, 2012, courtesy of Georg Raffelt)

tion to free streaming at their corresponding energy-averaged neutrinosphere. This sphere is also called transport sphere (sometimes also “scattering sphere”), whose radius $R_{V,t}$ is determined by solving Eq. (9) with a suitable spectral average of the total opacity $\kappa_{\text{tot}} \equiv \kappa_{\text{abs}} + \kappa_{\text{scatt}}$, which includes all contributions from scattering and absorption processes. Equilibration between neutrinos and the stellar background is possible up to the so-called average energy sphere (also termed “number sphere”, because outside of this location the number of neutrinos of a certain species is essentially fixed). When scatterings increase the zig-zag path of neutrinos diffusing through the medium and thus increase the probability of neutrinos to be absorbed, the radius $R_{V,e}$ of the energy sphere is given by the condition

$$\tau_{\text{eff}} = \int_{R_{V,e}}^{\infty} dr \rho \kappa_{\text{eff}} = \frac{2}{3} \quad (20)$$

(Shapiro and Teukolsky, 1983; Raffelt, 2001). Here, the effective optical depth is defined as

$$\kappa_{\text{eff}} = \sqrt{\kappa_{\text{abs}} \kappa_{\text{tot}}} . \quad (21)$$

In the integral of Eq. (20), again a suitable average of κ_{eff} over the energy spectrum has to be used. Since scattering and absorption contribute roughly equally to the total opacity of ν_e and $\bar{\nu}_e$, i.e., $\kappa_{\text{abs}} \approx (1/2) \kappa_{\text{tot}}$ and therefore $\kappa_{\text{eff}} \approx \kappa_{\text{tot}}/\sqrt{2} \sim (2/3) \kappa_{\text{tot}}$, the energy and transport sphere turn out to be nearly identical: $R_{\nu_e, e} \approx R_{\nu_e, t}$ and $R_{\bar{\nu}_e, e} \approx R_{\bar{\nu}_e, t}$ (see Fig. 4).

The situation is different for the heavy-lepton species ν_x . These are created and destroyed only as neutrino-antineutrino pairs in neutral-current reactions (cf. Fig. 3 and Table 1). While at high densities the main pair-production process is nucleon bremsstrahlung (with the plasmon-decay process contributing on a secondary level), electron-positron and $\nu_e \bar{\nu}_e$ annihilation take over as the dominant producers of $\nu_x \bar{\nu}_x$ pairs at densities below about 10% of nuclear matter density, where the stellar medium is less degenerate and larger numbers of positrons and electron antineutrinos are present. The total opacity of ν_x , however, is largely dominated by neutral-current scatterings off nucleons because of the much greater cross sections of these reactions. As a consequence, the average energy sphere of ν_x is located at considerably higher density, deeper inside the nascent neutron star, than their average transport sphere: $R_{\nu_x, e} < R_{\nu_x, t}$ (Fig. 4). While outside of the energy sphere the number flux of each species of ν_x is essentially conserved, the energy flux can still change between the energy and transport spheres because of energy transfers in the frequent collisions with nucleons (and to a lesser degree with electrons and electron-type neutrinos), in which mostly the energetic neutrinos from the high-energy tail of the ν_x spectrum can deliver energy to the cooler stellar medium (Raffelt, 2001; Keil et al, 2003).

The neutral-current nucleon scattering opacities of heavy-lepton neutrinos and antineutrinos are to lowest order the same (with only minor higher-order differences associated with weak-magnetism corrections Horowitz, 2002). In the absence of large concentrations of muons, also muon and tau neutrinos interact with the medium essentially symmetrically. For these reasons the four species of heavy-lepton neutrinos are treated as one kind of ν_x in many applications.

As the neutronization and deleptonization of the nascent neutron star progress due to the ongoing conversion of electrons and protons to neutrons and the escape of ν_e , the decreasing abundance of protons reduces the absorption opacity of $\bar{\nu}_e$. Therefore, as time goes on, the opacity of electron antineutrinos becomes more and more similar to that of heavy-lepton (anti)neutrinos, and the radiated spectra of these neutrinos match each other closely.

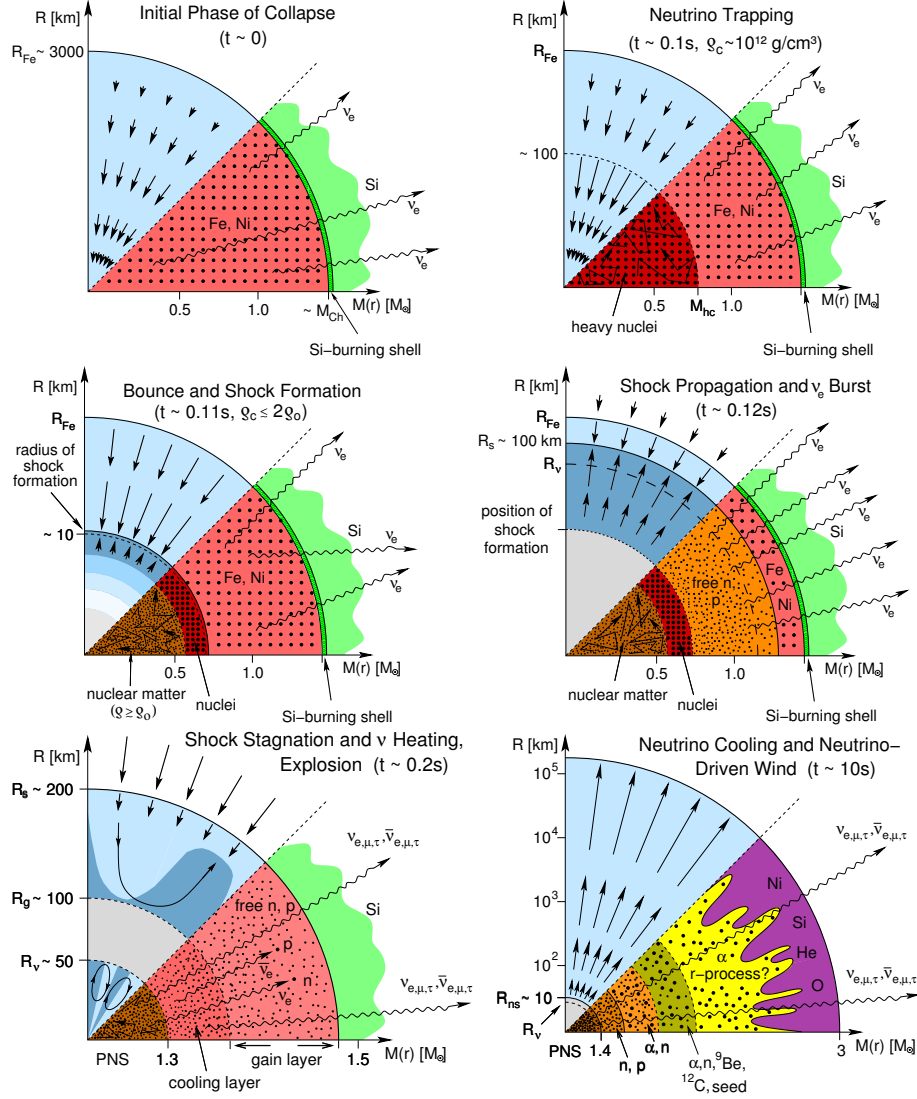


Fig. 5 Six phases of neutrino production and its dynamical consequences (from top left to bottom right). In the lower halves of the plots the composition of the stellar medium and the neutrino effects are sketched, while in the upper halves the flow of the stellar matter is shown by arrows. Inward pointing arrows denote contraction or collapse, outward pointing arrows expansion or mass ejection. Radial distances R are indicated on the vertical axes, the corresponding enclosed masses $M(r)$ are given on the horizontal axes. R_{Fe} , R_s , R_v , R_g , and R_{ns} denote the iron-core radius, shock radius, neutrinospheric radius, gain radius (which separates neutrino cooling and heating layers), and proto-neutron star (PNS) radius, respectively. M_{Ch} defines the effective Chandrasekhar mass, M_{hc} the mass of the homologously collapsing inner core (where velocity $u \propto r$), ρ_c the central density, and $\rho_0 \approx 2.7 \times 10^{14} \text{ g cm}^{-3}$ the nuclear saturation density. (Figure taken from Janka et al, 2007)

3 Neutrino Emission Phases

Figure 5 presents a series of plots that provide an overview of the main processes and regions of neutrino production and their dynamical effects during the collapse of a stellar core and on the way to the supernova explosion. Neutrinos exchange lepton number, energy and momentum with the stellar medium. Corresponding source terms must therefore be taken into account in the hydrodynamics equations that describe the time evolution of the stellar medium in terms of conservation laws for mass, momentum, energy, and (electron) lepton number.

(1) Onset of Stellar Core Collapse The slow contraction of the growing and aging iron core, which develops a progenitor-star dependent mass between $\sim 1.3 M_\odot$ and $\sim 2 M_\odot$, speeds up when its central temperature approaches 1 MeV ($\approx 10^{10}$ K). At this stage, thermal γ photons become sufficiently energetic to partially disintegrate the iron-group nuclei to α -particles and free nucleons. This converts thermal energy to rest-mass energy, thus overcoming the binding energy of nucleons in the nuclei, and causes a reduction of the effective adiabatic index, i.e., of the increase of the pressure with rising density, below the critical value of 4/3. (General relativistic effects lead to a slight upward correction of this critical value, rotation to a slight reduction.) Since the Fermi energy of the degenerate electrons also rises, electron captures on nuclei become possible (for the current state-of-the-art of the treatment, see Langanke et al, 2003; Juodagalvis et al, 2010; Balasi et al, 2015). Initially, the ν_e thus produced escape unimpeded (Fig. 5, top left panel).

(2) Neutrino Trapping When the density exceeds a few times $10^{11} \text{ g cm}^{-3}$, neutrinos begin to become trapped in the collapsing stellar core. From this moment on, the ν_e produced by ongoing electron captures—now dominantly on free protons—are swept inward with the infalling matter, and entropy as well as lepton number are essentially conserved in the contracting flow (Fig. 5, top right panel). Neutrino trapping is mainly a consequence of neutral-current scattering of low-energy neutrinos on heavy nuclei, whose nucleons act as one coherent scatterer. Because the vector parts of the neutrino-neutron scattering amplitudes dominate compared to those of protons (cf. Table 2) and add up in phase, whereas the overall axial-vector current is reduced by spin-pairing of the nucleons in nuclei, the coherent scattering cross section effectively scales with the square of the neutron number N :

$$\sigma_{A,\text{coh}} \approx \frac{1}{16} \sigma_0 \left(\frac{E}{m_e c^2} \right)^2 N^2. \quad (22)$$

As electrons continue to be converted to ν_e , the dynamical collapse accelerates to nearly free-fall velocities (up to $\sim 30\%$ of the speed of light) in the supersonic outer core region. The inner core implodes subsonically and homologously, i.e. with a velocity that is proportional to the radius, which implies a self-similar change of the structure. The size of the homologous core is roughly given by the instantaneous Chandrasekhar mass,

$$M_{\text{hc}} \lesssim M_{\text{Ch}} = 1.457 (2Y_e)^2 M_{\odot}, \quad (23)$$

where $Y_e = n_e/n_b$ is the number of electrons (number density n_e) per baryon (number density $n_b = n_p + n_n$). Since Y_e drops from an initial value around 0.46 for iron-group matter to less than 0.3 after trapping, the homologous core shrinks to roughly $0.5 M_{\odot}$ (Janka et al, 2012).

(3) Core Bounce and Shock Formation Within milliseconds after trapping, corresponding to the free-fall time,

$$t_{\text{ff}} \sim \frac{1}{\sqrt{G\rho}} \sim \frac{0.004}{\sqrt{\rho_{12}}} \text{ s} \quad (24)$$

(G being the gravitational constant and ρ_{12} the density in $10^{12} \text{ g cm}^{-3}$), the center reaches nuclear matter density, where the heavy nuclei dissolve in a phase transition to a uniform nuclear medium. A sharp rise of the incompressibility due to repulsive contributions to the nuclear force between the nucleons provides resistance against further compression, and the collapse of the homologous inner core comes to an abrupt halt. As it bounces back, sound waves steepen into a shock front at the boundary to the supersonically infalling outer layers (Fig. 5, middle left panel). The bounce shock begins to travel outwards against the ongoing collapse of the overlying iron-core material.

(4) Shock Propagation and ν_e Burst at Shock Breakout Electron neutrinos are produced in huge numbers by electron captures on free protons behind the outward moving shock front. However, they stay trapped in the dense postshock matter until the shock reaches sufficiently low densities for the ν_e to diffuse faster than the shock propagates. At this moment, the so-called shock breakout into neutrino-transparent layers, a luminous flash of ν_e –the breakout burst– is emitted (Fig. 5, middle right panel; Sect. 4.1).

Shortly after shock breakout, the dramatic loss of ν_e leads to a considerable drop of the electron-lepton number in the shock-heated matter. This allows for the appearance of large concentrations of positrons. Because of that and the compressional heating of the settling proto-neutron star, which begins to assemble around the center, pair-production processes (mainly e^-e^+ pair annihilation and nucleon bremsstrahlung; Table 1 and Fig. 3) become efficient and start to create heavy-lepton neutrinos and antineutrinos. With positrons and neutrons becoming more and more abundant, e^+ captures on neutrons also accomplish the emission of $\bar{\nu}_e$.

(5) Shock Stagnation and Revival by Neutrino Heating The shock front is a sharp flow discontinuity (whose narrow width is determined by the small, microphysical viscosity of the stellar plasma), in which the kinetic energy of the supersonically infalling preshock matter is dissipated into thermal energy, leading to an abrupt deceleration and compression of the flow and a corresponding increase of the density, temperature, pressure, and entropy behind the shock. Because of the temperature increase, heavy nuclei in the preshock medium are disintegrated essentially completely to free nucleons when the matter passes the shock. This consumes

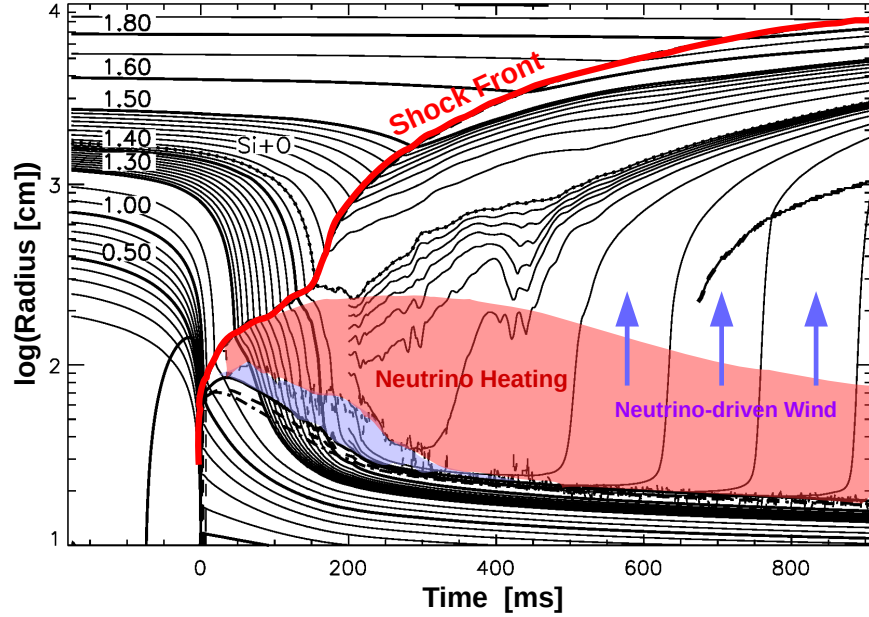


Fig. 6 Time evolution of the neutrino-driven explosion of a $15 M_{\odot}$ star as obtained in a multi-dimensional hydrodynamic simulation, visualized by a mass-shell plot. The horizontal axis shows time in milliseconds and the vertical axis the radial distance (in cm) on a logarithmic scale. The black, solid lines starting at the left edge of the plot belong to the radii that enclose selected values of baryonic mass, in some cases indicated by labels (in units of solar masses) next to the lines. The line with overlaid crosses marks the boundary between the silicon layer and the silicon-enriched oxygen layer of the progenitor star. Retreating lines signal the collapse of stellar shells and outgoing lines the expansion of matter expelled in the beginning supernova explosion. The thick red line marks the supernova shock front, which is formed at the moment of core bounce (here chosen to define time $t = 0$). The neutron star assembles from the mass shells settling in the lower part of the image at $t > 0$. The thick, black solid, dashed and dash-dotted lines that first expand and then contract with the neutron star represent the radial locations of the average neutrinospheres of ν_e , $\bar{\nu}_e$, and heavy-lepton neutrinos, respectively, close to the surface of the nascent neutron star. The light blue and red areas denote the regions of neutrino cooling and neutrino heating, respectively, outside of the neutrinospheres, which are separated by the “gain radius” (thin, dashed black line). The neutrino-driven wind (indicated by blue arrows) is visible by mass shells that start their outward expansion just above the neutron star surface. The thick-thin dashed line beginning at about 700 ms is the wind-termination shock that is formed when the fast wind collides with the slower preceding ejecta. (Figure adapted from Pruet et al, 2005)

appreciable amounts of energy, roughly 8.8 MeV per nucleon or 1.7×10^{51} erg per $0.1 M_{\odot}$. This energy drain and the additional energy losses by the ν_e -burst reduce the postshock pressure and weaken the expansion of the bounce shock. It finally stagnates at a radius of typically less than 150 km and an enclosed mass of around $1 M_{\odot}$, which is still well inside the collapsing stellar iron core. The prompt bounce-shock mechanism therefore fails to initiate the explosion of the dying star as supernova.

The most likely mechanism to revive the stalled shock front and to initiate its expansion against the ram pressure of the collapsing surrounding stellar core matter, is energy transfer by the intense neutrino flux radiated from the nascent neutron star. The most important reactions for depositing fresh energy behind the shock are ν_e and $\bar{\nu}_e$ captures on free nucleons:

$$\nu_e + n \longrightarrow p + e^-, \quad (25)$$

$$\bar{\nu}_e + p \longrightarrow n + e^+. \quad (26)$$

Current numerical simulations, recently also performed in all three spatial dimensions, demonstrate the viability of this neutrino-heating mechanism in principle (Fig. 6) so that this mechanism appears as the most promising explanation of the far majority of “normal” core-collapse supernovae. For stars more massive than $\sim 10 M_\odot$, non-radial hydrodynamic instabilities (like convective overturn and the standing accretion-shock instability (SASI)) provide crucial support for the onset of the explosion, and also for stars near the lower mass end of supernova progenitors ($\sim 9\text{--}10 M_\odot$), non-spherical flows play an important role for determining the energy and asymmetries of the explosion (see the indication of non-radial mass motions in the left bottom panel of Fig. 5). Despite the promising results of current models, many questions remain to be settled, and an ultimate confirmation of the neutrino-driven mechanism will require observational evidence. A high-statistics measurement of the neutrino signal from a future galactic supernova could be a milestone in this respect.

Before the supernova shock front re-accelerates outward and the supernova blast is launched, stellar matter collapsing through the stagnant shock feeds a massive accretion flow onto the nascent neutron star (typically several $0.1 M_\odot \text{ s}^{-1}$). The hot accretion mantle around the high-density, lower-entropy core of the neutron star radiates high fluxes mainly of ν_e and $\bar{\nu}_e$, which carry away the gravitational binding energy that is released in the gravitational collapse. This accretion luminosity adds to the core luminosity of all species of neutrinos and antineutrinos (ν_e , $\bar{\nu}_e$, and ν_x) that diffuse out from the deeper layers (Fig. 5, bottom left panel).

(6) Proto-neutron Star Cooling and Neutrino-driven Wind Accretion does not subside immediately after the explosion sets in. There can be an extended phase of continued mass accretion by the nascent neutron star that proceeds simultaneously to the outward acceleration of mass behind the outgoing shock. Eventually, however, after hundreds of milliseconds up to maybe a second, depending on the progenitor star and the speed of shock expansion, accretion ends and the proto-neutron star enters its Kelvin-Helmholtz cooling phase, in which it loses its remaining gravitational binding energy by the emission of neutrinos and antineutrinos of all flavors on the time scale of neutrino diffusion. Based on a simple diffusion model for a homogeneous sphere, Burrows (1984, 1990b) derived order-of-magnitude estimates for the deleptonization and energy-loss time scales:

$$t_L \sim \frac{3R_{\text{ns}}^2}{\pi^2 c \lambda_0} \frac{dY_L}{dY_{\nu_e}} \sim 3 \text{ s}, \quad (27)$$

$$t_E \sim \frac{3R_{\text{ns}}^2}{\pi^2 c \lambda_0} \frac{E_{\text{th}}^0}{2E_V^0} \sim 10 \text{ s}, \quad (28)$$

where $R_{\text{ns}} \approx 10 \text{ km}$ is the neutron-star radius,

$$\lambda_0 = \frac{1}{n_b \langle \sigma_V \rangle} \sim 10 \text{ cm} \left(\frac{E}{100 \text{ MeV}} \right)^{-2} \left(\frac{M_{\text{ns}}}{1.5 M_\odot} \right)^{-1} \left(\frac{R_{\text{ns}}}{10 \text{ km}} \right)^3 \quad (29)$$

the initial average mean free path of the neutrinos, E_{th}^0 and E_V^0 the initial total baryon and neutrino thermal energies, respectively, and the ratio of these thermal energies as well as dY_L/dY_{V_e} describe the ability of the neutron star to replenish the loss of lepton number and energy due to the radiated neutrinos from the available reservoirs of these quantities. While the temperatures in the interior of the newly formed neutron star can reach up to more than 50 MeV and the thermal energies of neutrinos can be 100 MeV and higher, these high-energy neutrinos are absorbed, re-emitted and downscattered billions of times before they escape from the neutrinospheric region with final mean energies of 10–20 MeV over much of the Kelvin-Helmholtz phase.

While the proto-neutron star deleptonizes and cools by neutrino losses, the energetic neutrinos radiated from the neutrinosphere continue to deposit energy in the overlying, cooler layers, mainly by the reactions of Eqs. (25) and (26). This leads to a persistent, dilute outflow of mass (with initial mass-loss rates of typically several $10^{-2} M_\odot \text{ s}^{-1}$) from the surface of the nascent neutron star. This so-called neutrino-driven wind (Fig. 5, bottom right panel, and Fig. 6) is discussed as potential site for the formation of trans-iron elements. The mass-loss rate, entropy, and expansion velocity of this wind are sensitive functions of the neutron-star radius and mass and of the luminosities and spectral hardness of the emitted neutrinos (Qian and Woosley, 1996; Otsuki et al, 2000; Thompson et al, 2001; Arcones et al, 2007). Even more important is the fact that the neutron-to-proton ratio of the expelled matter is determined by the luminosity and spectral differences of ν_e and $\bar{\nu}_e$, which leads to an interesting sensitivity of the nucleosynthetic potential of this environment to the nuclear physics of the neutron star medium and to non-standard neutrino physics like flavor oscillations or the speculative existence of sterile neutrinos.

4 Neutrino Emission Properties

Three main phases of neutrino emission can be discriminated that correspond to the dynamical evolution stages described in the previous section (Janka, 1993). They are displayed in Fig. 7 and described in the following three subsections.

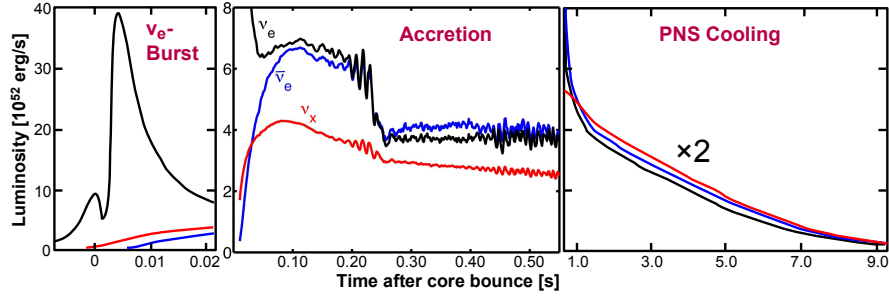


Fig. 7 Neutrino luminosities (ν_e : black; $\bar{\nu}_e$: blue; ν_x as one species of ν_μ , $\bar{\nu}_\mu$, ν_τ , $\bar{\nu}_\tau$: red) during the main neutrino-emission phases. The *left panel* shows the prompt burst of electron neutrinos associated with the moment of shock breakout into the neutrino-transparent outer core layers only milliseconds after bounce ($t = 0$). The *middle panel* corresponds to the post-bounce accretion phase before shock revival as computed in a three-dimensional simulation (see Tamborra et al, 2014). The quasi-periodic luminosity variations are a consequence of modulations of the mass-accretion rate by the neutron star caused by violent non-radial motions due to hydrodynamic instabilities (in particular due to the standing accretion-shock instability or SASI) in the postshock layer. The *right panel* displays the decay of the neutrino luminosities over several seconds in the neutrino-cooling phase of the newly formed neutron star (the plotted values are scaled up by a factor of 2)

4.1 Shock-breakout Burst of Electron Neutrinos

A luminous flash of neutronization neutrinos is radiated when the shock transitions from the opaque to the neutrino-transparent, low-density ($\rho \lesssim 10^{11} \text{ g cm}^{-3}$) outer layers of the iron core. At this moment, typically setting in ~ 2 ms after core bounce, the large number of ν_e created by electron captures on free protons in the shock-heated matter can ultimately escape. During the preceding collapse prior to core bounce, the ν_e emission rises continuously because an increasingly bigger fraction of the stellar core is compressed to densities where efficient electron captures become possible. Only within a brief period (± 1 ms) around core bounce, the strong compression and Doppler redshifting of the main region of ν_e generation lead to a transient dip in the ν_e luminosity. At shock breakout, also the luminosities of heavy-lepton neutrinos and shortly afterwards those of $\bar{\nu}_e$ begin to rise, because their production by pair processes becomes possible in the shock-heated matter (see Sect. 3; Fig. 7, left panel). The ν_e luminosity burst and the rise phase of the $\bar{\nu}_e$ and ν_x luminosities show a generic behavior with little dependence on the progenitor star (Kachelrieß et al, 2005). The burst reaches a peak luminosity near $4 \times 10^{53} \text{ erg s}^{-1}$, has a half-width of less than 10 ms and releases about $2 \times 10^{51} \text{ erg}$ of energy within only 20 ms. The mean energy of the radiated ν_e also peaks at the time of maximum luminosity and reaches 12–13 MeV (Figure 8, lower left panel).

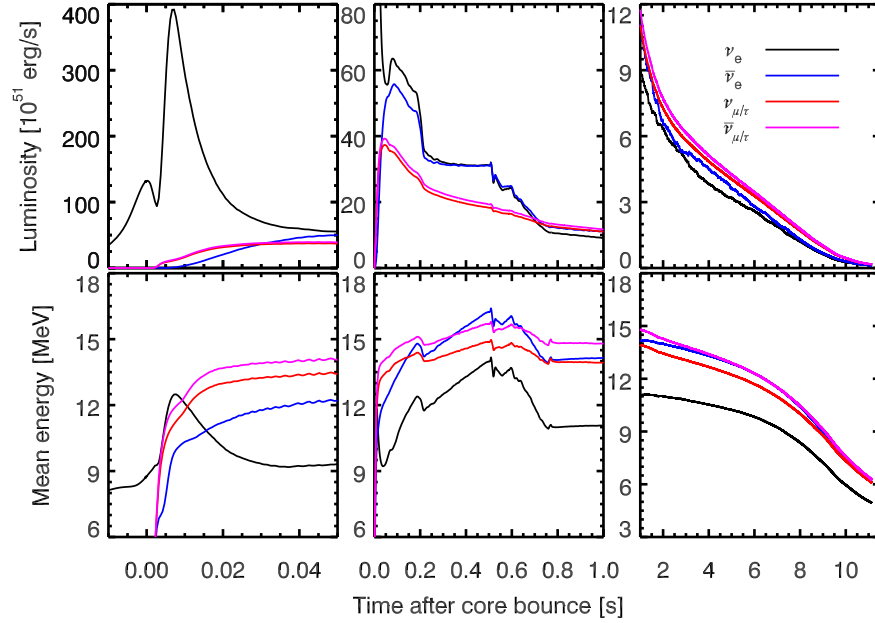


Fig. 8 Neutrino signal computed for the supernova explosion of a star of $27 M_{\odot}$, which gives birth to a neutron star with $1.6 M_{\odot}$. The *left panels* correspond to the shock-breakout phase, the *middle panels* to the post-bounce accretion phase including the transition to the proto-neutron star cooling phase, which is given in the *right panels*. The *upper panels* display the neutrino luminosities (ν_e black; $\bar{\nu}_e$ blue; one species of $\nu_{\mu,\tau}$: red; one species of $\bar{\nu}_{\mu,\tau}$: magenta), and the *lower panels* display the mean energies of the radiated neutrinos. In contrast to Fig. 7, the differences of heavy-lepton neutrinos and antineutrinos associated with weak-magnetism corrections of neutrino-nucleon scattering are shown. The slightly lower scattering opacity of $\bar{\nu}_{\mu,\tau}$ leads to slightly higher luminosities and higher mean energies (by ~ 1 MeV) compared to those of $\nu_{\mu,\tau}$. The explosion sets in at 0.5 s after core bounce, but accretion onto the proto-neutron star ends only at about 0.75 s, which marks the onset of the cooling phase. (Figure courtesy of Robert Bollig)

4.2 Post-bounce Accretion

This phase follows when the ν_e luminosity declines from the maximum and levels off into a plateau. Both ν_e and $\bar{\nu}_e$ are produced in large numbers by charged-current processes in the hot mantle of the proto-neutron star. The mass of this mantle grows continuously, because it is fed by the accretion flow of the collapsing stellar matter that falls through the stagnant shock and is heated by compression. The luminosities of ν_e and $\bar{\nu}_e$ are very similar during this phase with a slight number excess of ν_e because of ongoing deleptonization. In contrast, the individual luminosities of ν_x are considerably lower. These neutrinos originate mostly from the denser core region, where the high densities and temperatures allow nucleon bremsstrahlung to generate $\nu_x \bar{\nu}_x$ pairs.

The neutrino emission (luminosities and mean energies) during the accretion phase show large variations between different progenitor stars, because the neutrino quantities scale with the mass accretion rate, $\dot{M}(t)$, and the growing proto-neutron star mass, $M_{\text{ns}}(t)$. Both \dot{M} and M_{ns} are higher for progenitor stars that possess more compact cores, i.e., where a certain mass is condensed into a smaller volume prior to collapse. Progenitors with higher core compactness (which tend to be more massive, too, but with considerable non-monotonic variations) therefore radiate higher luminosities and harder neutrino spectra (Janka et al, 2012; O’Connor and Ott, 2013).

Moreover, non-radial flows in the supernova core, which are a consequence of hydrodynamic instabilities in the proto-neutron star and in the region behind the stalled shock front (like convective overturn and the standing accretion-shock instability (SASI)), can cause large-scale temporal modulations of the accretion flow onto the neutron star. This can lead to time- and direction dependent, large-amplitude, quasi-periodic fluctuations of the luminosities and mean energies of the radiated neutrinos during the accretion phase (Fig. 7, middle panel Lund et al, 2012; Tamborra et al, 2013, 2014).

The instantaneous spectra of the radiated muon and tau neutrinos are reasonably well described by Fermi-Dirac functions with zero degeneracy, and their luminosities can be expressed by a Stefan-Boltzmann like formula as

$$L_{\nu_x} = 4\pi\phi s_\nu R_{\text{ns}}^2 T_\nu^4, \quad (30)$$

where the average energy and the effective spectral temperature T_ν (measured in MeV) are linked by $\langle E \rangle = 3.15 T_\nu$. R_{ns} is the radius of the proto-neutron star and $s_\nu = 4.50 \times 10^{35} \text{ erg MeV}^{-4} \text{ cm}^{-2} \text{ s}^{-1}$ for a single species of ν_x . The “greyness factor” ϕ is determined by numerical simulations to range between ~ 0.4 and ~ 0.85 (Müller and Janka, 2014).

Since the emission of ν_e and $\bar{\nu}_e$ is enhanced by the accretion component, the sum of their luminosities can be written as

$$L_{\nu_e} + L_{\bar{\nu}_e} = 2\beta_1 L_{\nu_x} + \beta_2 \frac{GM_{\text{ns}}\dot{M}}{R_{\text{ns}}}. \quad (31)$$

The first term on the r.h.s. represents the “core component” of the luminosity carried by neutrinos diffusing out from the high-density inner regions of the proto-neutron star. This component can be assumed to be similar to the luminosity of ν_μ plus $\bar{\nu}_\mu$, because the core radiates all types of neutrinos in roughly equal numbers from a reservoir in thermal equilibrium, which is confirmed by the close similarity of the luminosities of all neutrino species after the end of accretion. The second term on the r.h.s. stands for the accretion component expressed by the product of mass accretion rate, \dot{M} , and Newtonian surface gravitational potential of the neutron star, $\Phi = GM_{\text{ns}}/R_{\text{ns}}$. By a least-squares fit to a large set of 1D results for the post-bounce accretion phase of different progenitor stars, values between $\beta_1 \approx 1.25$ and $\beta_2 \approx 0.5$ can be deduced (L. Hudepohl, 2014, private communication), which depend only weakly on the nuclear EoS. The values apply later than about 150 ms after bounce, when the postshock accretion layer has settled into a quasi-steady state. Müller and

Janka (2014) used a form slightly different from Eq. (31) with $\beta_1 = 1$; they found $\beta_2 \approx 0.5$ –1 prior to explosion.

During the accretion phase the mean energies of all neutrino species show an overall trend of increase, which is typically steeper for ν_e and $\bar{\nu}_e$ than for ν_x . The secular rise of the mean energies of the radiated ν_e and $\bar{\nu}_e$ is fairly well captured by the proportionality $\langle E_\nu \rangle \propto M_{\text{ns}}(t)$. The proportionality constant depends on the neutrino type but is only slightly progenitor-dependent (Müller and Janka, 2014). This secular rise of $\langle E_{\nu_e} \rangle$ and $\langle E_{\bar{\nu}_e} \rangle$ is supported by a local temperature maximum somewhat inside of the neutrinospheres of these neutrinos, which forms because of compressional heating of the growing accretion layer in progenitors with sufficiently high accretion rates (typically more massive than about $10 M_\odot$). Because of the continuous growth of the mean energies with $M_{\text{ns}}(t)$, the canonical order of the average energies, $\langle E_{\nu_e} \rangle < \langle E_{\bar{\nu}_e} \rangle < \langle E_{\nu_x} \rangle$ changes (transiently) to $\langle E_{\nu_e} \rangle < \langle E_{\nu_x} \rangle < \langle E_{\bar{\nu}_e} \rangle$ (Fig. 8, lower middle panel). This hierarchy inversion is enhanced and shifted to earlier times when energy transfer in neutrino-nucleon scattering is taken into account. Non-isoenergetic neutrino-nucleon scattering reduces the mean energies of ν_x in the “high-energy filter” layer between the ν_x energy sphere and the ν_x transport sphere (see Sect. 2.3 and Fig. 4 Raffelt, 2001; Keil et al, 2003). The corresponding energy transfer to the stellar medium also raises the luminosities and mean energies of ν_e and $\bar{\nu}_e$. Different from the mean energies, the mean squared energies, $\langle E_\nu^2 \rangle$, and rms energies always obey the canonical hierarchy.

4.3 Kelvin-Helmholtz Cooling and Deleptonization of the Proto-neutron Star

After the explosion has set in, the proto-neutron star continues to radiate lepton number and energy by high neutrino fluxes for many seconds (Sect. 3). The luminosities of all kinds of neutrinos and antineutrinos become similar (within $\sim 10\%$) during this phase and decline with time in parallel (Fig. 7, right panel). The typical average luminosities during Kelvin-Helmholtz cooling are of the order of

$$L_\nu^{\text{tot}} \equiv \sum_{i=e,\mu,\tau} L_{\nu_i} + L_{\bar{\nu}_i} \sim \frac{E_b}{t_E} \sim \text{several } 10^{52} \text{ erg s}^{-1}. \quad (32)$$

Rough estimates of E_b and t_E were provided by Eq. (1) and Eq. (28), respectively. Around about 1 second, the mean energies of the radiated neutrinos show a turnover and begin to decrease, reflecting the gradual cooling of the outer layers of the proto-neutron star (Fig. 8). A thick convective shell inside the star grows in mass while its inner boundary progresses towards the center (see Mirizzi et al, 2015). Convective energy transport in the high-density core of the neutron star is faster than diffusive transport and considerably accelerates the lepton number and energy loss through neutrinos. Because of the “high-energy filter” effect of the extended scattering atmosphere between the energy and transport spheres of heavy-lepton neutrinos, $\nu_{\mu,\tau}$

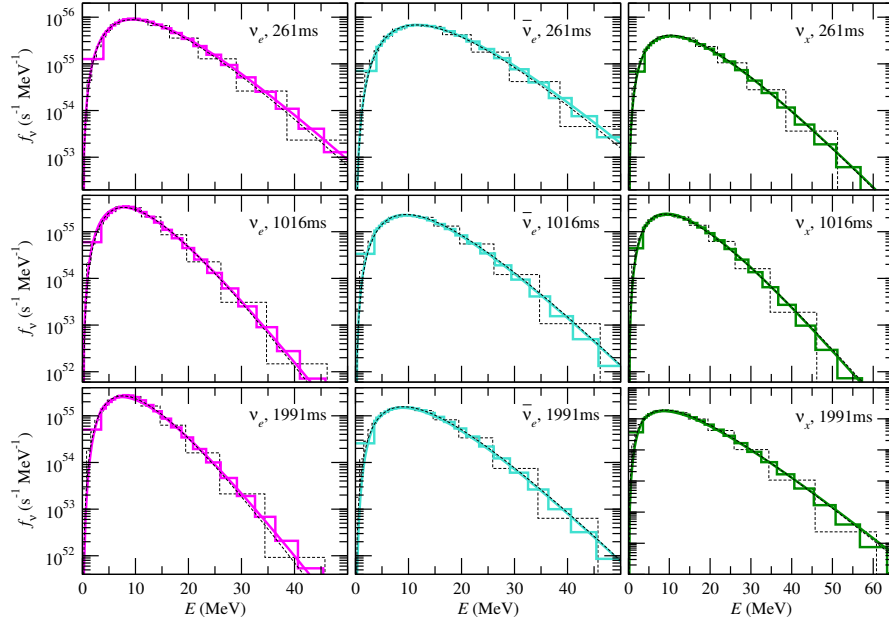


Fig. 9 Spectra for electron neutrinos (ν_e ; *left column*), electron antineutrinos ($\bar{\nu}_e$; *middle column*), and heavy-lepton neutrinos (ν_x , *right column*) during the accretion phase (261 ms after core bounce, *top row*) and for two times during the proto-neutron star cooling phase (1016 ms, *middle row*; 1991 ms, *bottom row*). The step functions are results of numerical simulations with lower (thin dashed) and higher (thick, colored) resolution. The continuous curves are quasi-thermal fits according to Eq. (33) for the lower resolution (thin dashed lines) and higher resolution (thick solid lines) cases. All α values for the fit functions are in the interval $2.3 \leq \alpha \leq 3.3$. (Figure taken from Tamborra et al, 2012)

with their higher scattering opacity are radiated with slightly softer spectra than $\bar{\nu}_e$ and $\bar{\nu}_{\mu,\tau}$ during all of the Kelvin-Helmholtz cooling evolution (Fig. 8, lower right panel).

4.4 Spectral Shape

The spectra of radiated neutrinos are usually somewhat different from thermal spectra. Since neutrino-matter interactions are strongly energy dependent, neutrinos of different energies decouple from the background medium at different radii with different temperatures of the stellar plasma. Nevertheless, the emitted neutrino spectrum can still be fitted by a Fermi-Dirac distribution, $f(E) \propto E^2 [1 + \exp(E/T - \eta)]^{-1}$, with fit temperature T (in energy units) and effective degeneracy parameter η (Janka and Hillebrandt, 1989). A mathematically more convenient representation was introduced by Keil et al (2003), who proposed the following di-

mensionless form for the energy distribution at a large distance from the radiating source:

$$f_\alpha(E) \propto \left(\frac{E}{\langle E \rangle} \right)^\alpha e^{-(\alpha+1)E/\langle E \rangle}, \quad (33)$$

where

$$\langle E \rangle = \frac{\int_0^\infty dE E f_\alpha(E)}{\int_0^\infty dE f_\alpha(E)} \quad (34)$$

is the average energy. The parameter α represents the amount of spectral “pinching” and can be computed from the two lowest energy moments of the spectrum, $\langle E \rangle$ and $\langle E^2 \rangle$, by

$$\frac{\langle E^2 \rangle}{\langle E \rangle^2} = \frac{2 + \alpha}{1 + \alpha}. \quad (35)$$

Higher energy moments $\langle E^\ell \rangle$ for $\ell > 1$ are defined analogue to Eq. (34) with E^ℓ under the integral in the numerator instead of E . Besides its analytic simplicity, this functional form has the advantage to also allow for the representation of a wider range of values for the spectral (anti-)pinching than a Fermi-Dirac fit. A Fermi-Dirac spectrum with vanishing degeneracy parameter ($\eta = 0$) corresponds to $\alpha \approx 2.3$, a Maxwell-Boltzmann spectrum to $\alpha = 2$, and $\alpha \gtrsim 2.3$ yields “pinched” spectra (i.e., narrower than a thermal Fermi-Dirac spectrum), whereas $\alpha \lesssim 2.3$ gives anti-pinched ones. Comparing to high-resolution transport results, Tamborra et al (2012) showed that these “ α -fits” also reproduce the high-energy tails of the radiated neutrino spectra very well (Fig. 9).

The shape parameter α is up to 6–7 for ν_e around the ν_e -burst, and in the range of 2–3 for all neutrino species at times later than ~ 200 ms after bounce (Mirizzi et al, 2015). In particular ν_e and $\bar{\nu}_e$ exhibit a tendency of pinched spectra. This spectral pinching can be understood as a consequence of the energy dependence of the neutrino interactions and can be exemplified by considering the radiated luminosity spectrum as a combination of thermal contributions from different, energy-dependent decoupling regions:

$$\frac{dL_\nu(E)}{dE} \approx \frac{1}{4} c (4\pi R_\nu^2(E)) B_\nu(E) \equiv \pi c R_\nu^2(E) \frac{4\pi}{(hc)^3} \frac{E^3}{1 + \exp[(E - \mu_\nu)/T]}, \quad (36)$$

with $T = T(R_\nu(E))$ and $\mu_\nu = \mu_\nu(R_\nu(E))$ being the gas temperature (in MeV) and neutrino equilibrium chemical potential at decoupling radius $R_\nu(E)$. The smaller interaction cross section and opacity of low-energy neutrinos (Eq. 8) lead to their energetic decoupling at a smaller radius (cf. Eq. 20), whereas high-energy neutrinos decouple at larger radii, where the stellar temperature is lower. These effects cause a reduction of the low-energy and high-energy wings on both sides of the spectral peak compared to a thermal spectrum with the temperature of the spectral maximum.

5 Conclusions

Theoretical predictions of the neutrino emission from supernovae have become considerably more reliable and detailed since improved transport treatments have become available in numerical simulations after the change of the millennium. This Chapter provides an overview of the foundations of the neutrino physics in collapsing stars. Moreover, it presents a summary of our current understanding of production and properties of the neutrino signal emitted during supernova explosions and the birth of neutron stars.

The most advanced methods for describing neutrino transport in computational supernova models in spherical symmetry apply solvers for the time-dependent Boltzmann transport equation (Liebendörfer et al, 2001, 2004; Lentz et al, 2012) or for the set of its first two moment equations with a variable Eddington factor closure derived from a simplified Boltzmann equation (Rampp and Janka, 2002; Müller et al, 2010). Both approaches take into account the velocity dependence of the neutrino transport, general relativistic effects, and the full phase-space dependence of the neutrino interaction rates summarized in Table 1 and Fig. 3. These most advanced codes have been shown to yield results of similar quality and overall consistency between each other (Liebendörfer et al, 2005; Marek et al, 2006; Müller et al, 2010). These methods constitute the present state-of-the-art for simulating neutrino transport in supernovae and proto-neutron stars in spherical symmetry.

In three-dimensional supernova modeling similar sophistication is not yet feasible. The current forefront here is defined by ray-by-ray implementations of the two-moment method with Boltzmann closure (Buras et al, 2006; Melson et al, 2015b,a) and of flux-limited diffusion (Lentz et al, 2015), and the application of two-moment schemes with algebraic closure relations is in sight. Solving the time-dependent Boltzmann transport problem in six-dimensional phase-space, however, is still on the far horizon and remains a challenging task for future supercomputing on the exascale level.

The same is true for a fully self-consistent inclusion of the effects of neutrino flavor transformations. Matter-background induced oscillations according to the Mikheyev-Smirnov-Wolfenstein (MSW) effect (Wolfenstein, 1978; Mikheyev and Smirnov, 1985) for the three active neutrino flavors occur at densities far below those of the supernova core (around 100 g cm^{-3} and at several 1000 g cm^{-3}) and must be taken into account when neutrinos propagate through the dying star on their way to the terrestrial detector. Since matter oscillations are suppressed in the dense interior at conditions far away from the MSW resonances (Wolfenstein, 1979; Hannestad et al, 2000), flavor mixing inside of the neutrinosphere can be safely ignored, unless fast pairwise neutrino conversions play a role (Izaguirre et al, 2017, and references therein). Outside of the neutrinosphere, however, the neutrino densities are so enormous that the large ν - ν interaction potential can trigger self-induced flavor conversions. The possible consequences of this interesting effect have so far been explored in post-processing studies using unoscillated neutrino data from numerical supernova simulations (for a status report, see Mirizzi et al, 2015). The highly complex and rich phenomenology of these self-induced flavor changes, how-

ever, is not yet settled, and therefore final conclusions on their possible effects for the supernova physics and for neutrino detection cannot be drawn yet.

The detection of a high-statistics neutrino signal from a supernova in the Milky Way is a realistic possibility with existing and upcoming experimental facilities. Such a measurement will provide unprecedentedly detailed and direct information of the physical conditions and of the dynamical processes that facilitate and accompany the collapse and explosion of a star and the formation of its compact remnant. A discovery of the diffuse supernova neutrino background as integrated signal of all past stellar collapse events seems to be in reach (for a review, see Mirizzi et al, 2015). It will put our fundamental understanding of the neutrino emission from the whole variety of stellar death events to the test and may offer the potential to set constraints on neutron star versus black hole formation rates.

Résumé Neutrinos are crucial agents during all stages of stellar collapse and explosion. Besides gravitational waves they are the only means to obtain direct information from the very heart of dying stars. Therefore they are a unique probe of the physics that plays a role at extreme conditions that otherwise are hardly accessible to laboratory experiments. The total energy, luminosity evolution, spectral distribution, and the mix of different species, which describe the radiated neutrino signal, carry imprints of the thermodynamic conditions, dynamical processes, and characteristic properties of the progenitor star and of its compact remnant. Numerical models are advanced to an increasingly higher level of realism for better predictions of the measurable neutrino features and their consequences.

Acknowledgements The author is indebted to Georg Raffelt for valuable discussions and thanks him and Robert Bollig for providing graphics used in this article. Research by the author was supported by the European Research Council through an Advanced Grant (ERC-AdG No. 341157-COCO2CASA), by the Deutsche Forschungsgemeinschaft through the Cluster of Excellence “Universe” (EXC-153), and by supercomputing time from the European PRACE Initiative and the Gauss Centre for Supercomputing.

Cross-References

Neutrino-driven Explosions

Neutrinos and Their Impact on Core-Collapse Supernova Nucleosynthesis

Neutrino Conversion in Supernovae

Neutrino Signatures from Young Neutron Stars

Explosion Physics of Core-Collapse Supernovae

Neutrinos from Core-Collapse Supernovae and Their Detection

The Diffuse Neutrino Flux from Supernovae

Gravitational Waves from Supernovae

References

- Alexeyev EN, Alexeyeva LN, Krivosheina IV, Volchenko VI (1988) Detection of the neutrino signal from SN 1987A in the LMC using the INR Baksan underground scintillation telescope. *Physics Letters B* 205:209–214, DOI 10.1016/0370-2693(88)91651-6
- Arcones A, Janka HT, Scheck L (2007) Nucleosynthesis-relevant conditions in neutrino-driven supernova outflows. I. Spherically symmetric hydrodynamic simulations. *Astron Astrophys* 467:1227–1248, DOI 10.1051/0004-6361:20066983, *astro-ph/0612582*
- Arnett WD (1966) Gravitational collapse and weak interactions. *Canadian Journal of Physics* 44:2553
- Balasi KG, Langanke K, Martínez-Pinedo G (2015) Neutrino-nucleus reactions and their role for supernova dynamics and nucleosynthesis. *Progress in Particle and Nuclear Physics* 85:33–81, DOI 10.1016/j.ppnp.2015.08.001, 1503.08095
- Bethe HA (1990) Supernova mechanisms. *Rev Mod Phys* 62:801–866, DOI 10.1103/RevModPhys.62.801
- Bionta RM, Blewitt G, Bratton CB, Casper D, Ciocio A (1987) Observation of a neutrino burst in coincidence with supernova 1987A in the Large Magellanic Cloud. *Physical Review Letters* 58:1494–1496, DOI 10.1103/PhysRevLett.58.1494
- Bruenn SW (1985) Stellar core collapse - Numerical model and infall epoch. *Astrophys J Suppl Ser* 58:771–841, DOI 10.1086/191056
- Buras R, Rampp M, Janka HT, Kifonidis K (2006) Two-dimensional hydrodynamic core-collapse supernova simulations with spectral neutrino transport. I. Numerical method and results for a $15 M_{\odot}$ star. *Astron Astrophys* 447:1049–1092, DOI 10.1051/0004-6361:20053783, *astro-ph/0507135*
- Burrows A (1984) On detecting stellar collapse with neutrinos. *Astrophys J* 283:848–852, DOI 10.1086/162371
- Burrows A (1990a) Neutrinos from supernova explosions. *Annual Review of Nuclear and Particle Science* 40:181–212, DOI 10.1146/annurev.ns.40.120190.001145
- Burrows A, Lattimer JM (1986) The birth of neutron stars. *Astrophys J* 307:178–196, DOI 10.1086/164405
- Burrows A, Young T, Pinto P, Eastman R, Thompson TA (2000) A New Algorithm for Supernova Neutrino Transport and Some Applications. *Astrophys J* 539:865–887, DOI 10.1086/309244, *astro-ph/9905132*
- Burrows A, Reddy S, Thompson TA (2006) Neutrino opacities in nuclear matter. *Nuclear Physics A* 777:356–394, DOI 10.1016/j.nuclphysa.2004.06.012, *astro-ph/0404432*
- Burrows AS (1990b) Neutrinos from supernovae. In: Petschek AG (ed) *Supernovae*, Springer, New York, pp 143–181
- Colgate SA, White RH (1966) The Hydrodynamic Behavior of Supernovae Explosions. *Astrophys J* 143:626, DOI 10.1086/148549
- Freedman DZ, Schramm DN, Tubbs DL (1977) The Weak Neutral Current and its Effects in Stellar Collapse. *Annual Review of Nuclear and Particle Science* 27:167–207, DOI 10.1146/annurev.ns.27.120177.001123
- Hannestad S, Janka HT, Raffelt GG, Sigl G (2000) Electron-, mu-, and tau-number conservation in a supernova core. *Phys Rev D* 62(9):093021, DOI 10.1103/PhysRevD.62.093021, *astro-ph/9912242*
- Hirata K, Kajita T, Koshiba M, Nakahata M, Oyama Y (1987) Observation of a neutrino burst from the supernova SN1987A. *Physical Review Letters* 58:1490–1493, DOI 10.1103/PhysRevLett.58.1490
- Horowitz CJ (2002) Weak magnetism for antineutrinos in supernovae. *Phys Rev D* 65(4):043001, DOI 10.1103/PhysRevD.65.043001, *astro-ph/0109209*
- Izaguirre I, Raffelt G, Tamborra I (2017) Fast Pairwise Conversion of Supernova Neutrinos: A Dispersion Relation Approach. *Physical Review Letters* 118(2):021101, DOI 10.1103/PhysRevLett.118.021101, 1610.01612

- Janka HT (1993) Neutrinos from type-II supernovae and the neutrino-driven supernova mechanism. In: Giovannelli F, Mannocchi G (eds) *Frontier Objects in Astrophysics and Particle Physics*, Società Italiana di Fisica, Bologna, p 345
- Janka HT, Hillebrandt W (1989) Neutrino emission from type II supernovae - an analysis of the spectra. *Astron Astrophys* 224:49–56
- Janka HT, Langanke K, Marek A, Martínez-Pinedo G, Müller B (2007) Theory of core-collapse supernovae. *Physics Reports* 442:38–74, DOI 10.1016/j.physrep.2007.02.002, *astro-ph/0612072*
- Janka HT, Hanke F, Hudepohl L, Marek A, Müller B, Obergaulinger M (2012) Core-collapse supernovae: Reflections and directions. *Progress of Theoretical and Experimental Physics* 2012(1):01A309, DOI 10.1093/ptep/pts067, 1211.1378
- Juodagalvis A, Langanke K, Hix WR, Martínez-Pinedo G, Sampaio JM (2010) Improved estimate of electron capture rates on nuclei during stellar core collapse. *Nuclear Physics A* 848:454–478, DOI 10.1016/j.nuclphysa.2010.09.012, 0909.0179
- Kachelrieß M, Tomàs R, Buras R, Janka HT, Marek A, Rampp M (2005) Exploiting the neutronization burst of a galactic supernova. *Phys Rev D* 71(6):063003, DOI 10.1103/PhysRevD.71.063003, *astro-ph/0412082*
- Keil MT, Raffelt GG, Janka HT (2003) Monte Carlo Study of Supernova Neutrino Spectra Formation. *Astrophys J* 590:971–991, DOI 10.1086/375130, *arXiv:astro-ph/0208035*
- Langanke K, Martínez-Pinedo G, Sampaio JM, Dean DJ, Hix WR, Messer OE, Mezzacappa A, Liebendörfer M, Janka HT, Rampp M (2003) Electron Capture Rates on Nuclei and Implications for Stellar Core Collapse. *Physical Review Letters* 90(24):241102, DOI 10.1103/PhysRevLett.90.241102, *astro-ph/0302459*
- Lentz EJ, Mezzacappa A, Messer OEB, Hix WR, Bruenn SW (2012) Interplay of Neutrino Opacities in Core-collapse Supernova Simulations. *Astrophys J* 760:94, DOI 10.1088/0004-637X/760/1/94, 1206.1086
- Lentz EJ, Bruenn SW, Hix WR, Mezzacappa A, Messer OEB, Endeve E, Blondin JM, Harris JA, Marronetti P, Yakunin KN (2015) Three-dimensional Core-collapse Supernova Simulated Using a $15 M_{\odot}$ Progenitor. *Astrophys J Lett* 807:L31, DOI 10.1088/2041-8205/807/2/L31, 1505.05110
- Liebendörfer M, Mezzacappa A, Thielemann FK (2001) Conservative general relativistic radiation hydrodynamics in spherical symmetry and comoving coordinates. *Phys Rev D* 63(10):104003, DOI 10.1103/PhysRevD.63.104003, *astro-ph/0012201*
- Liebendörfer M, Messer OEB, Mezzacappa A, Bruenn SW, Cardall CY, Thielemann FK (2004) A Finite Difference Representation of Neutrino Radiation Hydrodynamics in Spherically Symmetric General Relativistic Spacetime. *Astrophys J Suppl Ser* 150:263–316, DOI 10.1086/380191, *astro-ph/0207036*
- Liebendörfer M, Rampp M, Janka HT, Mezzacappa A (2005) Supernova Simulations with Boltzmann Neutrino Transport: A Comparison of Methods. *Astrophys J* 620:840–860, DOI 10.1086/427203, *astro-ph/0310662*
- Lund T, Wongwathanarat A, Janka HT, Müller E, Raffelt G (2012) Fast time variations of supernova neutrino signals from 3-dimensional models. *Phys Rev D* 86(10):105031, DOI 10.1103/PhysRevD.86.105031, 1208.0043
- Marek A, Dimmelmeier H, Janka HT, Müller E, Buras R (2006) Exploring the relativistic regime with Newtonian hydrodynamics: an improved effective gravitational potential for supernova simulations. *Astron Astrophys* 445:273–289, DOI 10.1051/0004-6361:20052840, *astro-ph/0502161*
- Melson T, Janka HT, Bollig R, Hanke F, Marek A, Müller B (2015a) Neutrino-driven Explosion of a 20 Solar-mass Star in Three Dimensions Enabled by Strange-quark Contributions to Neutrino-Nucleon Scattering. *Astrophys J Lett* 808:L42, DOI 10.1088/2041-8205/808/2/L42, 1504.07631
- Melson T, Janka HT, Marek A (2015b) Neutrino-driven Supernova of a Low-mass Iron-core Progenitor Boosted by Three-dimensional Turbulent Convection. *Astrophys J Lett* 801:L24, DOI 10.1088/2041-8205/801/2/L24, 1501.01961

- Mezzacappa A, Liebendörfer M, Cardall CY, Bronson Messer OE, Bruenn SW (2004) Neutrino Transport in Core Collapse Supernovae. In: Fryer CL (ed) *Astrophysics and Space Science Library*, Kluwer, Dordrecht, *Astrophysics and Space Science Library*, vol 302, pp 99–131, DOI 10.1007/978-0-306-48599-2_4
- Mikheyev SP, Smirnov AY (1985) Resonance enhancement of oscillations in matter and solar neutrino spectroscopy. *Yadernaya Fizika* 42:1441–1448
- Mirizzi A, Tamborra I, Janka HT, Saviano N, Scholberg K, Bollig R, Hudepohl L, Chakraborty S (2015) Supernova Neutrinos: Production, Oscillations and Detection. *ArXiv e-prints* 1508.00785
- Müller B, Janka HT (2014) A New Multi-dimensional General Relativistic Neutrino Hydrodynamics Code for Core-collapse Supernovae. IV. The Neutrino Signal. *Astrophys J* 788:82, DOI 10.1088/0004-637X/788/1/82, 1402.3415
- Müller B, Janka HT, Dimmelmeier H (2010) A New Multi-dimensional General Relativistic Neutrino Hydrodynamic Code for Core-collapse Supernovae. I. Method and Code Tests in Spherical Symmetry. *Astrophys J Suppl Ser* 189:104–133, DOI 10.1088/0067-0049/189/1/104, 1001.4841
- O’Connor E, Ott CD (2013) The Progenitor Dependence of the Pre-explosion Neutrino Emission in Core-collapse Supernovae. *Astrophys J* 762:126, DOI 10.1088/0004-637X/762/2/126, 1207.1100
- Otsuki K, Tagoshi H, Kajino T, Wanajo Sy (2000) General Relativistic Effects on Neutrino-driven Winds from Young, Hot Neutron Stars and r-Process Nucleosynthesis. *Astrophys J* 533:424–439, DOI 10.1086/308632, astro-ph/9911164
- Pruet J, Woosley SE, Buras R, Janka HT, Hoffman RD (2005) Nucleosynthesis in the Hot Convective Bubble in Core-Collapse Supernovae. *Astrophys J* 623:325–336, DOI 10.1086/428281, astro-ph/0409446
- Qian YZ, Woosley SE (1996) Nucleosynthesis in Neutrino-driven Winds. I. The Physical Conditions. *Astrophys J* 471:331, DOI 10.1086/177973, astro-ph/9611094
- Raffelt GG (1996) Stars as laboratories for fundamental physics: the astrophysics of neutrinos, axions, and other weakly interacting particles. University of Chicago Press, Chicago
- Raffelt GG (2001) Mu- and Tau-Neutrino Spectra Formation in Supernovae. *Astrophys J* 561:890–914, DOI 10.1086/323379, arXiv:astro-ph/0105250
- Raffelt GG (2012) Neutrinos and the stars. In: *Proceedings of the International School of Physics “Enrico Fermi”*, vol 182, pp 61–143, DOI doi:10.3254/978-1-61499-173-1-61, arXiv:astro-ph/1201.1637
- Rampp M, Janka HT (2002) Radiation hydrodynamics with neutrinos. Variable Eddington factor method for core-collapse supernova simulations. *Astron Astrophys* 396:361–392, DOI 10.1051/0004-6361:20021398, astro-ph/0203101
- Shapiro SL, Teukolsky SA (1983) *Black holes, white dwarfs, and neutron stars: The physics of compact objects*. Wiley, New York
- Tamborra I, Müller B, Hudepohl L, Janka HT, Raffelt G (2012) High-resolution supernova neutrino spectra represented by a simple fit. *Phys Rev D* 86(12):125031, DOI 10.1103/PhysRevD.86.125031, 1211.3920
- Tamborra I, Hanke F, Müller B, Janka HT, Raffelt G (2013) Neutrino Signature of Supernova Hydrodynamical Instabilities in Three Dimensions. *Physical Review Letters* 111(12):121104, DOI 10.1103/PhysRevLett.111.121104, 1307.7936
- Tamborra I, Raffelt G, Hanke F, Janka HT, Müller B (2014) Neutrino emission characteristics and detection opportunities based on three-dimensional supernova simulations. *Phys Rev D* 90(4):045032, DOI 10.1103/PhysRevD.90.045032, 1406.0006
- Thompson TA, Burrows A, Meyer BS (2001) The Physics of Proto-Neutron Star Winds: Implications for r-Process Nucleosynthesis. *Astrophys J* 562:887–908, DOI 10.1086/323861, astro-ph/0105004
- Tubbs DL, Schramm DN (1975) Neutrino Opacities at High Temperatures and Densities. *Astrophys J* 201:467–488, DOI 10.1086/153909

- Wolfenstein L (1978) Neutrino oscillations in matter. *Phys Rev D* 17:2369–2374, DOI 10.1103/PhysRevD.17.2369
- Wolfenstein L (1979) Neutrino oscillations and stellar collapse. *Phys Rev D* 20:2634–2635, DOI 10.1103/PhysRevD.20.2634